JACS
JOURNAL OF THE AMERICAN CHEMICAL SOCIETY

Article

pubs.acs.org/JACS

A General Salt-Templating Method To Fabricate Vertically Aligned Graphitic Carbon Nanosheets and Their Metal Carbide Hybrids for Superior Lithium Ion Batteries and Water Splitting

Jixin Zhu, Ken Sakaushi, Guylhaine Clavel, Menny Shalom, Markus Antonietti, and Tim-Patrick Fellinger*

Department of Colloid Chemistry, Max Planck Institute of Colloids and Interfaces, 14424 Potsdam, Germany

Supporting Information

ABSTRACT: The synthesis of vertically aligned functional graphitic carbon nanosheets (CNS) is challenging. Herein, we demonstrate a general approach for the fabrication of vertically aligned CNS and metal carbide@CNS composites via a facile salt templating induced self-assembly. The resulting vertically aligned CNS and metal carbide@CNS structures possess ultrathin walls, good electrical conductivity, strong adhesion, excellent structural robustness, and small particle size. In electrochemical energy conversion and storage such unique features are favorable for providing efficient mass transport as well as a large and accessible electroactive surface. The materials were tested as electrodes in a lithium ion battery and in electrochemical water splitting. The vertically aligned nanosheets exhibit remarkable lithium ion storage properties and, concurrently, excellent properties as electrocatalysts for hydrogen evolution.

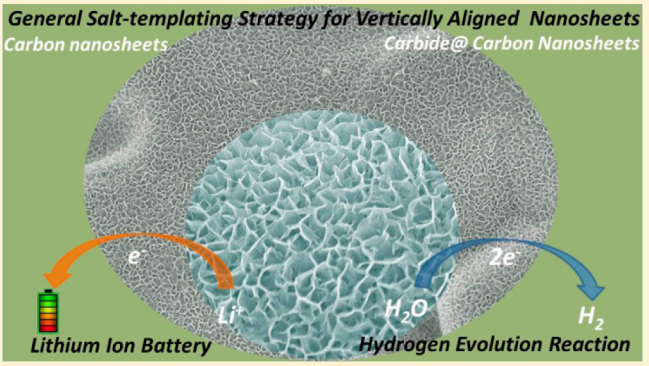

1. INTRODUCTION

Energy conversion and storage, in particular solar cells, fuel cells, and lithium ion batteries, become increasingly important to quickly meet the requirements of our societal development. Within these, lithium-ion batteries (LIBs) have been considered as one of the most promising electric energy storage systems, because of their advantages of high energy density, long lifespan, low cost, and environmental friendliness.[1,2] Hydrogen, as a clean and renewable energy resource, has been widely investigated as an alternative to the diminishing fossil fuels due to its high gravimetric energy density. In this regard, electrochemical water splitting has attracted tremendous interest as a clean technology that enables the conversion of intermittent renewable wind and solar energy into storable chemical energy (i.e., H_2, CO_2 fuels).[3,4] Great efforts have been devoted to explore effective strategies to design advanced electrode materials and electrocatalysts with high activity, low costs, and excellent stability for LIBs and water splitting.[4−7] Various groups work on optimization and engineering of reasonable structures, such as atomically thin layers, hybrid architectures, and element doping via various approaches including wet-chemical and thermochemical approaches.[8−11] Alternative strategies for the synthesis of cost-effective and highly efficient electrode materials for LIBs and water splitting are however still very desirable.

Two-dimensional (2D) materials, especially graphene and its derivatives, have attracted much attention due to their utilization as versatile building blocks for constructing a range of multifunctional three-dimensional (3D) architectures for electronics, catalysis, and energy conversion and storage.[12−14] The electrochemical properties of 2D materials and their hybrids are dependent on their intrinsic crystalline texture and electric conductivity, alongside their morphologies, compositions, and nature of exposed surfaces.[10,15−17] In particular, it was found that vertically aligned graphitic carbon nanosheets (CNS) exhibit excellent electrochemical energy storage properties owing to the merits of a large electrode electrolyte interface and strong interaction with the current collector, i.e. low contact resistance and optimized conduction pathways.[18,19] Enhancement of the catalytic performance in the hydrogen evolution reaction was also achieved employing vertically aligned nanosheet electrodes.[20] However, most of these vertically aligned 2D nanosheets were grown using chemical vapor deposition with relatively high technical requirements (e.g., PECVD) or made by multistep processes. Herein, we report on a novel and versatile salt-templating strategy for the synthesis of vertically aligned 2D nanosheets including N-doped CNS and metal carbides (e.g., $MoC_{0.654}$, WC, TaC, NbC)@N-doped CNS). It will be shown that these vertically aligned nanosheets exhibit largely enhanced lithium storage properties and also that they are well-performing electrocatalysts for the hydrogen evolution reaction.

Received: February 6, 2015
Published: April 8, 2015

DOI: 10.1021/jacs.5b01072
J. Am. Chem. Soc. 2015, 137, 5480−5485

2. RESULTS AND DISCUSSION

The synthesis of vertically aligned N-doped CNS and metal carbide@N-doped graphitic CNS (for convenience abbreviated as MC@CNS) mainly involves two steps as shown in Figure 1

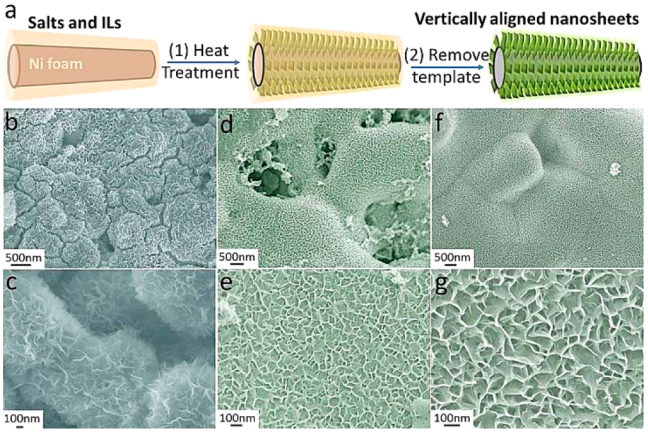

Figure 1. (a) Schematic illustration of the salt-templating process for the formation of vertically aligned two-dimensional (2D) nanosheets and typical field emission scanning electron microscopy (FESEM) images of nitrogen doped graphitic carbon nanosheets and $MoC_{0.654}$@CNS prepared at 900 °C for 3 h: (b–c) carbon nanosheets (CNS), (d–e) $MoC_{0.654}$@CNS1, and (f–g) $MoC_{0.654}$@CNS2.

(for details see Experimental Section in the Supporting Information). The precursor 1-ethyl-3-methylimidazolium dicyanamide (Emim-dca) and the salt mixture ($ZnCl_2$ and KCl with a mass ratio of 1:6) were thoroughly mixed and drop coated onto a commercial nickel foam support with a geometric surface area of 1 cm^2. Recently ionic liquid carbon precursors were frequently used because of their favorable handling and the interesting properties of the related carbons.[21−24] However, vertically aligned graphitic carbon nanosheet arrays have not been reported from these precursors. Here, vertically aligned CNS were obtained after thermal treatment in an inert gas atmosphere of the mixture at 900 °C for 3 h and subsequent removal of salt by washing with aqueous diluted HCl and deionized (DI) water. For the synthesis of MC@CNS, additional precursor metal salts ($MoCl_6$, WCl_5, $TaCl_5$, or $NbCl_5$) can be added to the mixture of Emim-dca and the salt template. MC@CNS were obtained after thermal treatment in an inert gas atmosphere of the mixture at 900 °C and the above-described washing procedure. Note that the simplicity of the described salt melt method is favorable in terms of scalability.

The morphology of as-prepared vertically aligned CNS and MC@CNS were systematically investigated by field-emission scanning electron microscopy (FE-SEM). With the above-described procedure, highly interconnected films, composed of vertically aligned nanosheets, were obtained after heat treatment at 900 °C for 3 h (Figure 1). High-resolution SEM imaging reveals that the thin nanosheets have lateral dimensions of 100–200 nm. The as-prepared CNS strongly adhere on the nickel foam, as the structure remains unchanged after washing and after ultrasonication for 1 h.

Our preliminary results suggest two main reasons for the formation of the vertically aligned CNS on nickel foam: (1) Nickel under reaction conditions can dissolve high amounts of carbon, which undergoes recrystallization from the surface to form graphitic carbon. The formation of carbon without an oriented structure from the carbonization/graphitization of polymer ionic liquid precursors and Fe-species as reactants was observed earlier in a bulk experiment.[25] Orientation therefore comes from the directional growth distal to the surface. (2) The $ZnCl_2$/KCl salt mixture acts as a porogen leading to separated flat structures. Recently, $ZnCl_2$ based salt melts gained attention as facile porogens for bottom-up syntheses.[24,26,27] SEM images of the products before removal of the salt are shown in Figure S1 (Supporting Information). The surface of the raw product is relatively smooth, and no sheets can be observed because of the embedding salt crust. The CNS can easily be liberated from the salt by aqueous washing. It can be clearly seen that the CNS are free-standing on the surface of nickel foam from the cross section SEM images (Figure S2, Supporting Information). For mechanistic considerations two blind experiments were performed. First, the precursor–salt mixture was equivalently carbonized without the nickel foam substrate. In this case an aerogel-like product consisting of interconnected nanospheres is obtained in ∼40% yield (Figure S3, Supporting Information). Second, the ionic liquid precursor was wetted on the nickel foam and carbonized in the absence of the inorganic salt. Instead of nanosheets we obtained bamboo-like carbon nanotubes (Figure S4, Supporting Information). These results emphasize the importance of the nickel surface for heterogeneous nucleation and graphitization via the dissolution/precipitation mechanism, whereas the preferential growth of CNS is aided by the presence of an inorganic salt melt. Otherwise, only 2D carbon nanosheets (in case of very high salt fractions) or porous carbon was obtained by the carbonization of an organic carbon source (e.g., glucose) in the presence of inorganic salts, however without observation of vertically aligned structures due to a different formation mechanism.[28] Figure 1d–g show some representative FESEM images of the obtained hybrid products from using $MoCl_6$ salt as an added precursor with different weight ratios of $MoCl_6$ to the $ZnCl_2$/KCl mixture. As in the case of CNS, the nickel foam scaffold was fully covered with vertically aligned nanosheets with a lateral size in the range of 100–200 nm. The morphology of the products obtained in the presence of $MoCl_6$ is similar to the as-prepared pure CNS, even for different relative amounts of the $MoCl_6$ precursor, which indicates the versatility of the structure formation mechanism. This is also evident from SEM observation of the reference samples before salt removal, the cross-sectional view, and the products with aerogel-like morphology obtained without a nickel substrate (Figures S1–S3, Supporting Information). Moreover, it is known that carbonization of ionic liquids in the presence of titanium and/or vanadium salts can lead to hybrids of carbon aerogel with TiN, VN, or mixed TiN/VN nanoparticles in one step.[29]

X-ray diffraction and Raman spectroscopy measurements were performed to gain further insight into the crystallinity and composition of the as-prepared CNS (Figure S5, Supporting Information). The diffractogram for CNS shows three main reflections originating from the nickel substrate and one peak located at around 26.6° ascribed to the (002) peak of graphitic carbon, whereas no other crystalline impurities were detected in the CNS sample. Raman scattering spectroscopy shows three well-resolved peaks at 1348, 1575, and 2682 cm^{-1} which are characteristic for the D, G, and 2D bands, further evidencing the formation of graphitic CNS. In addition, a weak D′ band located at ∼1619 cm^{-1} is observed. This is well-known to go along with nitrogen doping (see Supporting Information Figure S5b, inset).[30] The low intensity of the D band (which is also

DOI: 10.1021/jacs.5b01072
J. Am. Chem. Soc. 2015, 137, 5480–5485

influenced by heteroatom doping) at least indicates the relatively high degree of order in the as-prepared carbon nanosheets. In contrast, the aerogel product obtained without using the nickel foam substrate shows significantly broader Raman bands and no clear 2D band, which proves the comparably low order and the significance of the nickel foam to generate largely sp^2-hybridized, i.e. graphitic, carbon (Figure S6, Supporting Information). The crystallinity and composition of $MoC_{0.654}$@CNS products are further confirmed by the corresponding X-ray diffractogram and/or Raman scattering spectrum (Figure S5, Supporting Information). Besides the nickel and the graphitic carbon (002) peaks, the diffraction peaks located at 35.8°, 36.8°, 39.5°, 42.6°, and 48.6° can be well assigned to hexagonal $MoC_{0.654}$ (JCPDS 04-13-5834), which is consistent with characteristics of the product from the direct heat treatment of precursors without the nickel foam substrate (Figure S6, Supporting Information). In the case of $MoC_{0.654}$@CNS1 and $MoC_{0.654}$@CNS2, Raman scattering shows the same structural features of N-doped graphitic carbon as observed for the CNS samples. X-ray Photoelectron Spectroscopy (XPS) spectra show the characteristic satellites of Mo^0 (blue), Mo^{3+} (green), Mo^{4+} (yellow), and Mo^{6+} (red) with 3d5/2 and 3d3/2 bands (Figure S7, Supporting Information), which is consistent with reports on molybdenum carbides.[31] The N 1s band is also displayed, indicating the presence of an N dopant with a content of 3.1 wt %. Compared to the reference materials, the presence of nickel in all cases led to stronger Raman characteristics for graphitic carbon with well-developed D, G, and especially 2D band positions. Importantly, this is independent of the armoring of $MoC_{0.654}$ particles with graphite corroborating the formation of more graphitic carbon due to the nickel foam substrate. Without nickel foam, even in the presence of molybdenum salt, less-ordered nitrogen doped carbons are generated. Specific surface areas of randomly oriented CNS, and $Mo_{0.654}$C@CNS_2 and WC@CNS_samples, were determined by the BET method as shown in Figure S8 (Supporting Information). The surface area values are 89, 123, and 95 $m^3\ g^{-1}$ corresponding to CNS and CNS/$Mo_{0.654}$C. The content of the $MoC_{0.654}$ in the hybrids are estimated to be 32 wt % by thermogravimetric analysis (TGA, Figure S5c) from room temperature to 700 °C in air, where the product collected from heat treatment of the samples at 500 °C in air is examined by XRD (Figure S5d) and confirmed to be the MoO_3 [JCPDS 01-074-7912]. Additionally, the content of $MoC_{0.654}$ can be easily tuned to 40.4 wt % by changing the precursor ratio. In the following, the $MoC_{0.654}$@CNS with 32 and 40.4 wt % $MoC_{0.654}$ are denoted as $MoC_{0.654}$@CNS_1 and $MoC_{0.654}$@CNS_2, respectively. Figure S9 (Supporting Information) shows the TEM images of the pure CNS. It can be clearly observed that they consist of interconnected carbon nanosheets. The high-resolution TEM demonstrates the electron beam transparent character of the nanosheets which further evidences the thin feature of the carbon nanosheets. Figure 2 shows typical transmission electron microscopy (TEM) images of detached nanosheets after intense ultrasonication in ethanol. The thin nanosheets (~5 nm) are composed of graphite armored small nanoparticles with an average size of ~5 nm (Figure 2c) in diameter. The particles are embedded in a carbon matrix, which presumably complies with that of bare CNS.

The particles are single crystals and possess clear lattice fringes (Figure 2d). In the fast Fourier transform (FFT) pattern obtained from the corresponding HR-TEM image, the lattice

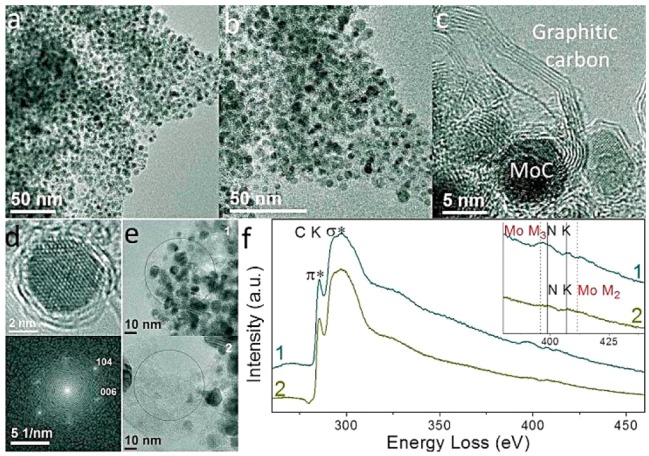

Figure 2. (a–c) Transmission electron microscopy (TEM) images of a typical $MoC_{0.654}$@CNS nanosheet, (d) high-resolution TEM image of a typical $MoC_{0.654}$ nanoparticle in $MoC_{0.654}$@CNS and the associated diffraction pattern generated by fast Fourier transformation (FFT), (e–f) TEM images and electron energy loss spectra (EELS) acquired from the regions shown in Figure 2e.

fringes of the planes were measured to be 0.246 and 0.212 nm corresponding well with the spacing of the (104) and (006) planes (010 zone axis) of hexagonal $MoC_{0.654}$. Electron energy loss spectra (EELS) acquired from the regions shown in Figure 2f further confirm the nitrogen doping within the carbon nanosheets, and the N content is estimated to be 3.3 wt %. This is in good agreement with results from elemental analysis and XPS results. It is to emphasize that the dissolution/reprecipitation mechanism to form carbon typically goes along with quantitative nitrogen loss. The present N doping is highly desired, because of the favorable properties of nitrogen doped carbons. In order to study the potential of the synthesis route to design different functional materials, selected transition metal salts (e.g., WCl_5, $TaCl_5$, and $NbCl_4$) were added to the otherwise equivalent procedure followed by carbonization at 900 °C under the same conditions. Remarkably, vertically aligned 2D nanosheets of WC@CNS, TaC@CNS, and NbC@CNS can be fabricated after simply using WCl_5, $TaCl_5$, and $NbCl_5$ as precursors. Again, all FESEM images of the products exhibit similar features in shape, size, and uniformity for the W, Ta, and Nb carbides as shown in Figure 3. Phases and crystal structures of the products were determined by XRD as shown in Figure S10 (Supporting Information), and the results reveal

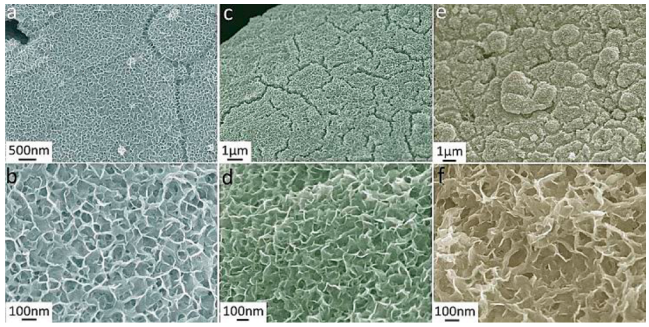

Figure 3. Typical field emission scanning electron microscopy (FESEM) images of MC@CNS using WCl_5, $TaCl_5$, and $NbCl_5$ as additional precursors: (a–b) WC@CNS), (c–d) TaC@CNS, and (c–d) NbC@CNS.

DOI: 10.1021/jacs.5b01072
J. Am. Chem. Soc. 2015, 137, 5480–5485

the formation of WC@CNS, TaC@CNS, and NbC@CNS, respectively. The TEM images of WC@CNS also demonstrate that uniform WC nanoparticles with an average size of 3 nm were embedded in the carbon nanosheets (Figure S8, Supporting Information). This further demonstrates the versatility of the presented method for the fabrication of vertically aligned nanosheet architectures of desired composition.

The unique structural features of the vertically aligned CNS and MC@CNS, including strong interaction with the substrate, ultralow thickness, good structural robustness, small particle size, and porous structure, render large electrode/electrolyte contact and short electron/ion diffusion pathways, when the materials are used as electrode materials. As a proof of concept, lithium storage properties were investigated using $MoC_{0.654}$@CNS as anode material for lithium ion batteries (Figure 4). For

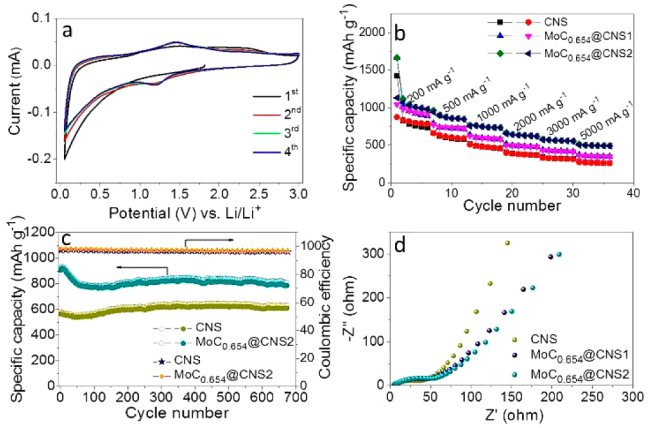

Figure 4. Electrochemical performances of CNS, $MoC_{0.654}$@CNS1, and $MoC_{0.654}$@CNS2. (a) Representative CV curve of $MoC_{0.654}$@CNS2 at a scan rate of 0.5 mV s^{-1} for the first four cycles; (b) the rate capability of CNS, $MoC_{0.654}$@CNS1, and $MoC_{0.654}$@CNS2 at current densities from 200 to 5000 mA g^{-1}; (c) cycling performance and coulombic efficiency of CNS, $MoC_{0.654}$@CNS1, and $MoC_{0.654}$@CNS2 at a current density of 500 mA g^{-1}; (d) Nyquist plots of CNS, $MoC_{0.654}$@CNS1, and $MoC_{0.654}$@CNS2 obtained over the frequency range 100 kHz to 0.01 Hz by applying a sine wave with an amplitude of 5.0 mV.

calculation of specific capacities, both carbon and molybdenum carbide phases together were considered as active material. In the representative cyclic voltammogram (CV), we obtained two redox couples located at around 0.1/0.3 V, 1.2/1.45 V and an oxidation shoulder at ~2.0 V vs Li/Li^+ (at 0.5 mV s^{-1}). These are considered to reflect intercalation into the CNS (e.g., $xLi^+ + C$ (CNS) + $xe^- \rightarrow Li_xC$) and conversion/alloying reactions of Li^+ with the $MoC_{0.654}$ phase (e.g., $yLi^+ + Mo_{0.654}C + ye^- \rightarrow Mo + Li_yC$) (Figure 4a), which would be in agreement with the recent report on lithium storage in molybdenum carbide.[32−36] Notably, the redox peaks of the bare vertically aligned CNS electrode are located at 0.1/0.3 V, but also at higher potentials in the range of 0.7/1.0 V and 1.5/2.0 V vs Li/Li^+. Supported by the charge−discharge profiles (Figure S11, Supporting Information) the redox peaks at lower potentials contribute to the overall capacity, mostly in the case of bare CNS. Accordingly theses peaks can be assigned to the intercalation of Li^+ into graphitic carbon. Nevertheless the mechanism behind the redox phenomena at higher potentials can herein not clearly be assigned, as pronounced redox regions can also be observed for the bare CNS electrode. One possible explanation is the formation of the solid electrolyte interface (SEI) layer from the electrolyte, e.g. ethylene carbonate (EC) and dimethyl carbonate (DMC), and a polymeric gel-type layer at high potential.[37] The cycling responses of $MoC_{0.654}$@CNS with different $MoC_{0.654}$ contents were evaluated at different current densities (Figure 4b). Throughout the whole cycle no clear plateaus can be observed. This can be explained by the comparably unordered structure of the graphitic carbon nanosheets on one hand. On the other hand lattice distortions throughout the intercalation in small nanoparticles may give rise to an unclear phase transition, whereas this behavior is in agreement with alloying and conversion reactions.

The first discharge capacity is around 1667 mAh g^{-1}, whereas the consecutive charge capacity is around 1133 mAh g^{-1}. This corresponds to an initial coulombic efficiency of 68%, where the capacity loss is commonly attributed to the formation of a solid electrolyte interface (SEI).[38] An average capacity as high as 1010 mAh g^{-1} is retained at a current density of 200 mA g^{-1}, while a capacity of 495 mAh g^{-1} is maintained even at a larger current density of 5 A g^{-1}. This clearly shows the advantageous effects of optimized conduction pathways and low contact resistance between the nickel back-electrode and the active CNS. To evaluate the relative contributions of carbon and metal carbide subphases, we also analyzed the bare CNS electrode, which still gives very high capacities of 800 and 265 mAh g^{-1} at the corresponding current densities of 200 mA g^{-1} and 5 A g^{-1}. These results imply CNS and MC@CNS exhibit excellent overall capacity and rate capability as anode materials for LIBs. Cycling performances of both systems were further studied at a current density of 500 mA g^{-1} (Figure 4c). The discharge capacity of the CNS electrode even slightly increases from 580 to 648 mAh g^{-1} at the 280th cycle, while this value is maintained to 680 cycles with a coulombic efficiency of 98%. This behavior is likely caused by formation of the SEI, accompanied by Li^+ ion capture, resulting in a small capacity loss. Remarkably, the $MoC_{0.654}$@CNS electrode retains its higher capacity of 815 mAh g^{-1} at least for 680 cycles. To reveal the reason for the excellent electrochemical behavior of such electrodes, electrochemical impedance spectroscopy (EIS) was carried out over a frequency range of 100 kHz to 0.01 Hz. Judging from the diameters of the semicircles and referring to the Randles circuit, the bare vertically aligned CNS electrode shows the smallest charge transfer resistance as compared to those of the $MoC_{0.654}$@CNS. The semicircles are not closed indicating high double layer capacities for each of the rough electrodes. However, all the samples are at comparably high levels of conductivity (Figure 4d). We attribute this to a high inherent electric conductivity and strong interaction between the vertically aligned active materials with the current collector in these binder-free electrodes. The increased phase shift angle (>45°) in the case of the bare CNS shows that this electrode behaves more like a capacitor with a reduced contribution of solid state diffusion as compared to the molybdenum carbide hybrids. The relatively high specific capacity of the CNS electrode ($C_{theo.}$(graphite) = 372 mAh g^{-1}) is therefore partly explainable by double layer capacity effects in addition to the lithium intercalation; i.e., Li ions are surface bound, together with their corresponding counter-electron in the carbon sheet. Generally, the structure enables quick transportation of both electrons and ions. This has been confirmed by the Li^+ storage performance of randomly oriented nanosheet samples as shown in Figure S12 (Supporting Information). The randomly

DOI: 10.1021/jacs.5b01072
J. Am. Chem. Soc. 2015, 137, 5480−5485

oriented CNS and $Mo_{0.654}C$/CNS samples show lower specific capacities, 470 and 610 mAh g^{-1}, which decay with the cycles more quickly, suggesting reduced cyclability. This is attributed to reduced charge transfer rates by weaker attachment to the current collector and the resistance of PVDF binder. The overall mesoscale architecture is apparently favorable for providing easy access for the electrolyte to the structure and short diffusion lengths of Li^+ within the materials. Additionally, the graphitic carbon layers on the surface of $Mo_{0.654}C$ small nanoparticles may effectively alleviate the lattice strain of $Mo_{0.654}C$ during the charging/discharging process.

To further illustrate the advantages of the present unique structure, the electrocatalytic activity of the as-prepared MC@CNS toward the electrochemical hydrogen evolution reaction (HER) was studied. A typical three-electrode electrochemical cell configuration using 0.1 M KOH aqueous solution as the electrolyte was employed (Figure 5). It was found that the

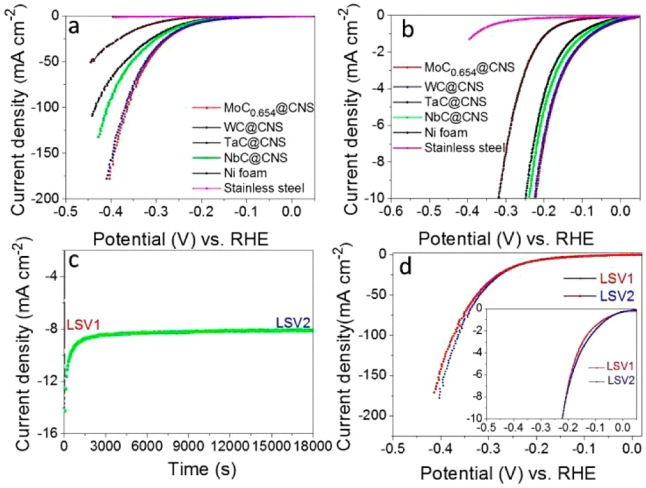

Figure 5. Electrocatalytic activities for hydrogen evolution reaction (HER). (a–b) The HER polarization curves for CNS, MC@CNSs, pure nickel foam, and the bare stainless steel electrode (electrolyte: 0.1 M KOH, scan rate: 1 mVs^{-1}); (c) stability profile of $MoC_{0.654}$@CNS1 electrode tested at a constant potential of −0.22 V for 5 h (loss resulting mostly from adsorbed bubbles); (d) polarization curves recorded for $MoC_{0.654}$@CNS before and after the stability testing at a constant potential of −0.22 V for 5 h.

$MoC_{0.654}$@CNS, WC@CNS, TaC@CNS, and NbC@CNS samples exhibited high activity for HER in alkaline medium, giving small corresponding benchmarking overpotentials η_{10} of 220, 220, 250, and 240 mV at a current density of 10 mA cm^{-2}. These overpotentials are much lower than that of pure Ni foam (320 mV). The obtained characteristics, especially in the case of tantalum and niobium carbide, compare favorably with other reported values (e.g., 250 mV at $j = -3$ mA cm^{-2} for $MoC_{0.654}$; 300 mV at $j = -10$ mA/cm^{-2} for WC; ∼325 mV at $j = -0.5$ mA cm^{-2} for TaC; and ∼275 mV at $j = -0.6$ mA cm^2 for NbC), although also better performing tungsten and molybdenum carbides were reported.[31,39−44] $MoC_{0.654}$@CNS and WC@CNS can deliver very high current densities of 180 and 178 mA cm^{-2} respectively at a low overpotential of 400 mV, rendering great potential as alternative electrocatalysts for water splitting. Because of the high practical relevance, the electrocatalysts' stability is exemplarily studied on $MoC_{0.654}$@CNS. Chronoamperometric testing was performed for 5 h at a constant potential of −0.22 V vs RHE (Figure 5c). The current density of the sample gradually decreases from −12 to −8.1 mA cm^{-2} and is stable after 50 min to 5 h. Importantly, the loss in current density is not due to catalyst degradation, but can mainly be attributed to generated bubbles partly covering the electrode surface. The catalytic HER performance of $MoC_{0.654}$@CNS in terms of polarization curves was therefore retested after 5 h of stability testing and removal of the bubbles. Interestingly, the former benchmarking overpotential η_{10} of 220 mV was still observed at the current density of 10 mA cm^{-2} (Figure 5d).

This stability of $MoC_{0.654}$@CNS is considered to result from the combined chemical and structural features of all subphases in MC@CNS, again rendering a very large but stable contact area of electrode/electrolyte and a high electrochemical activity of the small, carbon-armored nanoparticles. The electrocatalytic activity of randomly oriented $Mo_{0.654}C$@CNS and WC@CNS nanosheet samples was tested under the same conditions to reveal the structural advantages of these vertically aligned nanosheets on nickel foam as electrodes (Figure S13, Supporting Information). The randomly oriented $Mo_{0.654}C$@CNS and WC@CNS nanosheet samples give corresponding benchmarking overpotentials η_{10} of 280 and 290 mV at a current density of 10 mA cm^{-2}, which are 60 and 70 mV larger than those of their vertically aligned nanosheets samples. This is attributed to the worse electron transportation and the decrease in electric conductivity by Nafion binder. Remarkably, these values are still lower than that of pure nickel foam, which is ascribed to the high electrochemical activities of the metal carbides small particles.

3. SUMMARY

In summary, a general and scalable salt-melt based synthesis has been explored for the synthesis of vertically aligned two-dimensional nitrogen doped carbon nanosheets on a nickel foam substrate. The versatile approach allows for fabrication of the carbon nanostructures and a range of hybrid materials, which have metal carbide nanoparticles rigidly embedded into the graphitic carbon nanosheets. Owing to the structural merits of high electric conductivity, strong substrate interaction, thin transversal extension, and small particle size, the resulting two-dimensional nanosheets not only demonstrate high specific capacities and a long lifespan as anode materials in lithium ion batteries but also exhibit high activity and stability as the catalyst for the electrochemical hydrogen evolution reaction.

■ ASSOCIATED CONTENT

Ⓢ Supporting Information

Experimental details, SEM, TEM, XRD, Raman, TGA, XPS, CV, and charge−discharge profiles. This material is available free of charge via the Internet at http://pubs.acs.org.

■ AUTHOR INFORMATION

Corresponding Author

*Tim.Fellinger@mpikg.mpg.de

Notes

The authors declare no competing financial interest.

■ ACKNOWLEDGMENTS

The authors wish to thank the Fritz Haber Institute of the Max Planck Society for the TEM support. Carmen Serra from C.A.C.T.I./Universidad de Vigo is acknowledged for XPS measurements. We would also like to thank the technical staff

DOI: 10.1021/jacs.5b01072
J. Am. Chem. Soc. 2015, 137, 5480−5485

at MPIKG for performing service measurements such as elemental analysis, TGA.

REFERENCES

(1) Kang, B.; Ceder, G. *Nature* **2009**, *458*, 190.
(2) Armstrong, A. R.; Lyness, C.; Panchmatia, P. M.; Islam, M. S.; Bruce, P. G. *Nat. Mater.* **2011**, *10*, 223.
(3) Tian, J.; Liu, Q.; Asiri, A. M.; Sun, X. *J. Am. Chem. Soc.* **2014**, *136*, 7587.
(4) Li, Y.; Wang, H.; Xie, L.; Liang, Y.; Hong, G.; Dai, H. *J. Am. Chem. Soc.* **2011**, *133*, 7296.
(5) Lee, S. W.; Yabuuchi, N.; Gallant, B. M.; Chen, S.; Kim, B.-S.; Hammond, P. T.; Shao-Horn, Y. *Nat. Nanotechnol.* **2010**, *5*, 531.
(6) Wu, H.; Chan, G.; Choi, J. W.; Ryu, I.; Yao, Y.; McDowell, M. T.; Lee, S. W.; Jackson, A.; Yang, Y.; Hu, L.; Cui, Y. *Nat. Nanotechnol.* **2012**, *7*, 310.
(7) Chen, S.; Duan, J.; Jaroniec, M.; Qiao, S. Z. *Angew. Chem., Int. Ed.* **2013**, *52*, 13567.
(8) Zhu, C.; Yu, Y.; Gu, L.; Weichert, K.; Maier, J. *Angew. Chem., Int. Ed.* **2011**, *50*, 6278.
(9) Fan, G.; Li, F.; Evans, D. G.; Duan, X. *Chem. Soc. Rev.* **2014**, *43*, 7040.
(10) Song, F.; Hu, X. *Nat. Commun.* **2014**, *5*, 4477.
(11) Gao, M. R.; Yao, W.-T.; Yao, H. B.; Yu, S. H. *J. Am. Chem. Soc.* **2009**, *131*, 7486.
(12) Zheng, Y.; Jiao, Y.; Chen, J.; Liu, J.; Liang, J.; Du, A.; Zhang, W.; Zhu, Z.; Smith, S. C.; Jaroniec, M.; Lu, G. Q.; Qiao, S. Z. *J. Am. Chem. Soc.* **2011**, *133*, 20116.
(13) Zhu, C.; Zeng, Z.; Li, H.; Li, F.; Fan, C.; Zhang, H. *J. Am. Chem. Soc.* **2013**, *135*, 5998.
(14) Tan, C.; Qi, X.; Liu, Z.; Zhao, F.; Li, H.; Huang, X.; Shi, L.; Zheng, B.; Zhang, X.; Xie, L.; Tang, Z.; Huang, W.; Zhang, H. *J. Am. Chem. Soc.* **2015**, *137*, 1565.
(15) Zhu, X.; Zhu, Y.; Murali, S.; Stoller, M. D.; Ruoff, R. S. *ACS Nano* **2011**, *5*, 3333.
(16) Subbaraman, R.; Tripkovic, D.; Strmcnik, D.; Chang, K. C.; Uchimura, M.; Paulikas, A. P.; Stamenkovic, V.; Markovic, N. M. *Science* **2011**, *334*, 1256.
(17) Gong, M.; Li, Y.; Wang, H.; Liang, Y.; Wu, J. Z.; Zhou, J.; Wang, J.; Regier, T.; Wei, F.; Dai, H. *J. Am. Chem. Soc.* **2013**, *135*, 8452.
(18) Miller, J. R.; Outlaw, R. A.; Holloway, B. C. *Science* **2010**, *329*, 1637.
(19) Bo, Z.; Zhu, W.; Ma, W.; Wen, Z.; Shuai, X.; Chen, J.; Yan, J.; Wang, Z.; Cen, K.; Feng, X. *Adv. Mater.* **2013**, *25*, 5799.
(20) Kong, D.; Wang, H.; Cha, J. J.; Pasta, M.; Koski, K. J.; Yao, J.; Cui, Y. *Nano Lett.* **2013**, *13*, 1341.
(21) Lee, J. S.; Wang, X. Q.; Luo, H. M.; Baker, G. A.; Dai, S. *J. Am. Chem. Soc.* **2009**, *131*, 4596.
(22) Fechler, N.; Fellinger, T. P.; Antonietti, M. *J. Mater. Chem. A* **2013**, *1*, 14097.
(23) Fellinger, T. P.; Hasche, F.; Strasser, P.; Antonietti, M. *J. Am. Chem. Soc.* **2012**, *134*, 4072.
(24) Fellinger, T.-P.; Thomas, A.; Yuan, J.; Antonietti, M. *Adv. Mater.* **2013**, *25*, 5838.
(25) Yuan, J.; Giordano, C.; Antonietti, M. *Chem. Mater.* **2010**, *22*, 5003.
(26) Antonietti, M.; Fechler, N.; Fellinger, T. P. *Chem. Mater.* **2013**, *26*, 196.
(27) Elumeeva, K.; Fechler, N.; Fellinger, T. P.; Antonietti, M. *Mater. Horiz.* **2014**, *1*, 588.
(28) Liu, X.; Giordano, C.; Antonietti, M. *Small* **2014**, *10*, 193.
(29) Fechler, N.; Fellinger, T. P.; Antonietti, M. *Chem. Mater.* **2012**, *24*, 713.
(30) Ci, L.; Song, L.; Jin, C.; Jariwala, D.; Wu, D.; Li, Y.; Srivastava, A.; Wang, Z. F.; Storr, K.; Balicas, L.; Liu, F.; Ajayan, P. M. *Nat. Mater.* **2010**, *9*, 430.
(31) Wan, C.; Regmi, Y. N.; Leonard, B. M. *Angew. Chem., Int. Ed.* **2014**, *53*, 6407.
(32) Yang, S.; Feng, X.; Wang, L.; Tang, K.; Maier, J.; Müllen, K. *Angew. Chem., Int. Ed.* **2010**, *49*, 4795.
(33) Mukhopadhyay, A.; Guo, F.; Tokranov, A.; Xiao, X.; Hurt, R. H.; Sheldon, B. W. *Adv. Funct. Mater.* **2013**, *23*, 2397.
(34) Gao, Q.; Zhao, X.; Xiao, Y.; Zhao, D.; Cao, M. *Nanoscale* **2014**, *6*, 6151.
(35) Naguib, M.; Halim, J.; Lu, J.; Cook, K. M.; Hultman, L.; Gogotsi, Y.; Barsoum, M. W. *J. Am. Chem. Soc.* **2013**, *135*, 15966.
(36) Eames, C.; Islam, M. S. *J. Am. Chem. Soc.* **2014**, *136*, 16270.
(37) Lucas, I. T.; Pollak, E.; Kostecki, R. *Electrochem. Commun.* **2009**, *11*, 2157.
(38) Yang, S.; Gong, Y.; Liu, Z.; Zhan, L.; Hashim, D. P.; Ma, L.; Vajtai, R.; Ajayan, P. M. *Nano Lett.* **2013**, *13*, 1596.
(39) Liu, Q.; Tian, J.; Cui, W.; Jiang, P.; Cheng, N.; Asiri, A. M.; Sun, X. *Angew. Chem., Int. Ed.* **2014**, *53*, 6710.
(40) Vrubel, H.; Hu, X. *Angew. Chem., Int. Ed.* **2012**, *51*, 12703.
(41) Garcia-Esparza, A. T.; Cha, D.; Ou, Y.; Kubota, J.; Domen, K.; Takanabe, K. *ChemSusChem* **2013**, *6*, 168.
(42) Liao, L.; Wang, S.; Xiao, J.; Bian, X.; Zhang, Y.; Scanlon, M. D.; Hu, X.; Tang, Y.; Liu, B.; Girault, H. H. *Energy Environ. Sci.* **2014**, *7*, 387.
(43) Liu, Y.; Kelly, T. G.; Chen, J. G.; Mustain, W. E. *ACS Catal.* **2013**, *3*, 1184.
(44) Tomás-García, A. L.; Jensen, J. O.; Bjerrum, N. J.; Li, Q. *Electrochim. Acta* **2014**, *137*, 639.

DOI: 10.1021/jacs.5b01072
J. Am. Chem. Soc. 2015, 137, 5480−5485